The Astrophysical Journal, 793:15 (10pp), 2014 September 20 doi:10.1088/0004-637X/793/1/15

DISTRIBUTION OF ELECTRIC CURRENTS IN SUNSPOTS FROM PHOTOSPHERE TO CORONA

Sanjay Gosain[1], Pascal Démoulin[2], and Marcelo López Fuentes[3]
[1] National Solar Observatory, 950 North Cherry Avenue, Tucson, AZ 85719, USA
[2] Observatoire de Paris, LESIA, UMR 8109 (CNRS), F-92195 Meudon Principal Cedex, France
[3] Instituto de Astronomía y Física del Espacio (IAFE), UBA-CONICET, CC. 67, Suc. 28 Buenos Aires 1428, Argentina
Received 2014 February 12; accepted 2014 July 28; published 2014 August 29

ABSTRACT

We present a study of two regular sunspots that exhibit nearly uniform twist from the photosphere to the corona. We derive the twist parameter in the corona and in the chromosphere by minimizing the difference between the extrapolated linear force-free field model field lines and the observed intensity structures in the extreme-ultraviolet images of the Sun. The chromospheric structures appear more twisted than the coronal structures by a factor of two. Further, we derive the vertical component of electric current density, j_z, using vector magnetograms from the *Hinode* Solar Optical Telescope (SOT). The spatial distribution of j_z has a zebra pattern of strong positive and negative values owing to the penumbral fibril structure resolved by *Hinode*/SOT. This zebra pattern is due to the derivative of the horizontal magnetic field across the thin fibrils; therefore, it is strong and masks weaker currents that might be present, for example, as a result of the twist of the sunspot. We decompose j_z into the contribution due to the derivatives along and across the direction of the horizontal field, which follows the fibril orientation closely. The map of the tangential component has more distributed currents that are coherent with the chromospheric and coronal twisted structures. Moreover, it allows us to map and identify the direct and return currents in the sunspots. Finally, this decomposition of j_z is general and can be applied to any vector magnetogram in order to better identify the weaker large-scale currents that are associated with coronal twisted/sheared structures.

Key words: magnetic fields – Sun: chromosphere – Sun: corona – Sun: photosphere – sunspots

Online-only material: color figures

1. INTRODUCTION

The observations of the coronal loops and chromospheric fibrils above solar active regions often show the presence of twisted structures. Structures such as X-ray sigmoids (Rust & Kumar 1996; Green et al. 2011) and H_α super-penumbral whorls (Nakagawa et al. 1971; Balasubramaniam et al. 2004) suggest a twisted magnetic field topology. Some observed configurations have structures susceptible to be modeled with a linear force-free field (LFFF). This provides us with an estimate of the force-free parameter $\alpha = \boldsymbol{J}/\boldsymbol{B}$, where $\boldsymbol{J} = \nabla \times \boldsymbol{B}/\mu_0$ is the electric current density. For example, the modeling of the coronal and the chromospheric structures with LFFF has been attempted in the past to study X-ray sigmoids (Pevtsov et al. 1997; Mandrini et al. 2005) and also to infer relative magnetic helicity in the corona (Mandrini et al. 2004; Nakwacki et al. 2011).

The magnetic field threading the solar chromosphere and the lower corona is believed to be nearly force-free. This assumption is generally true at these heights as the plasma β parameter (β = gas pressure/magnetic pressure) is much less than unity (Gary 2001) and the structures are believed to be in quasi-static equilibrium. The magnetic field measurement in the corona is very difficult as the corona is optically thin, spectral lines are thermally broadened, and the magnetic field strength is very weak (Lin et al. 2000). Therefore, direct magnetic field measurements are mostly confined to the photospheric and in very few cases to the chromospheric heights (Harvey 2012), and one resorts to force-free field extrapolation methods to reconstruct three-dimensional coronal magnetic fields.

The computation of the LFFF in the corona requires only the longitudinal component of the magnetic field in the photosphere as the boundary condition (Schmidt 1964; Semel 1967). In addition, the coronal images are used to constrain the model field (Green et al. 2002; Démoulin et al. 1997). The linear force-free parameter α of the LFFF model is typically estimated by comparing/fitting reconstructed field lines to the coronal structures, in the least-squares sense. On the other hand, with photospheric vector magnetograms one can directly compute the distribution of the force-free parameter α at the photospheric boundary. Since the coronal field is an extension of the photospheric field, a similar value of α is expected due to the balance of torque between the photospheric and the coronal parts of the flux tube (Longcope & Welsch 2000; Chae et al. 2003). Indeed, Burnette et al. (2004) found that the value of α derived for the coronal field by LFFF modeling corresponds well with the mean value of the photospheric distribution of α.

However, the plasma β becomes larger than unity as one approaches the photospheric layers and therefore plasma forces cannot be neglected, i.e., the field may not be completely force-free. Therefore, a correspondence between the α distribution from photospheric vector magnetograms and the best-fit α in the corona and chromosphere from LFFF modeling need not be guaranteed a priori. Nevertheless, in a large number of cases studied by Pevtsov et al. (1997), a good correspondence was found between the α deduced from vector magnetograms and LFFF modeling of X-ray sigmoids. This study led them to propose that the origin of twist in the coronal structures is of subsurface origin. This correspondence further suggests that (1) the force-free assumption for photospheric magnetic field is not completely wrong, and (2) electric currents in the corona are a continuation of the vertical component of the electric currents deduced at the photospheric level from vector magnetograms.

Although photospheric flux is argued to be organized in the form of fibrils (Spruit 1979; Parker 1984), i.e., isolated flux tubes with zero net currents, such fibril structure has not been resolved by previous magnetographs. Parker (1996) had argued

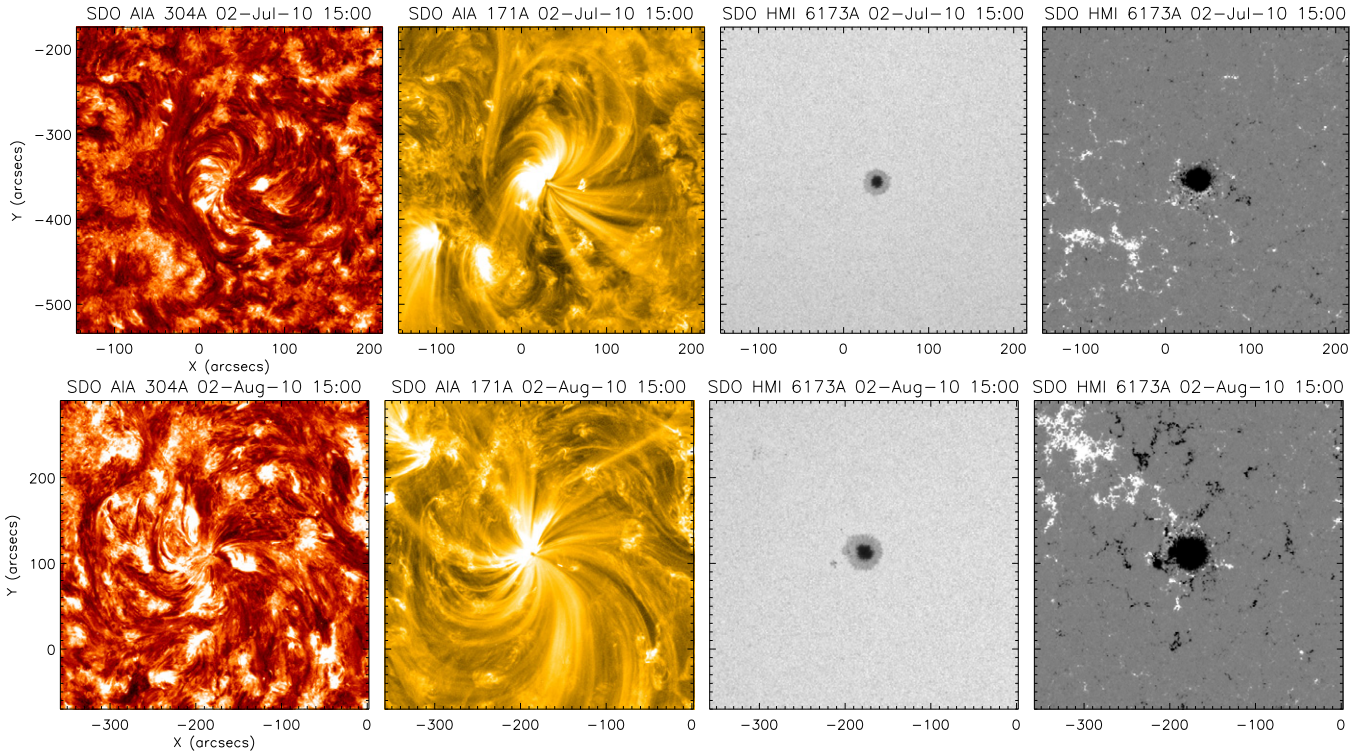

Figure 1. Context images of the two sunspots, NOAA 11084 and 11092, obtained by *SDO*/AIA, are shown in the top and bottom row, respectively. The images from left to right show, respectively, the filtergrams in AIA 304 Å and 171 Å channels, photospheric continuum intensity map, and longitudinal magnetogram from HMI. The AIA 304 Å and 171 Å images have been contrast enhanced by applying a high-pass filter.

(A color version of this figure is available in the online journal.)

that if sunspots are formed of clusters of such fibrils, then the net currents in sunspots should also be zero.

However, using vector magnetograms of active regions, statistical studies of the average value of current helicity, $H_c = J_z \cdot B_z$, and of the force-free parameter $\alpha = J_z/B_z$ (where z refers to local vertical) show a hemispheric predominance of negative sign of these parameters in the northern hemisphere and positive sign in the southern hemisphere (Seehafer 1990; Pevtsov et al. 1994; Abramenko et al. 1996; Bao & Zhang 1998; Gosain et al. 2013). These observed statistics suggest that currents are not neutralized, i.e., the so-called direct current is not balanced by the return current (Wheatland 2000). Such cases are also present in magnetohydrodynamic (MHD) simulations when a finite magnetic shear is present along the photospheric inversion line between magnetic polarities (see Figure 9 and related text in Aulanier et al. 2005). This is the case in an MHD simulation of an emerging twisted flux tube studied by Török et al. (2014), since the flux tube has neutralized currents below the photosphere but develops un-neutralized currents in the corona. Observationally also, such non-neutralized current systems were reported by Ravindra et al. (2011) near the polarity inversion line (PIL) in a δ sunspot.

In this paper we present a study of two sunspots whose high-resolution chromospheric and coronal images show whirly structures. These whirly structures suggest a nearly azimuthal symmetry. We separately model the structures in the corona and chromosphere above these sunspots with the LFFF approximation and derive force-free parameters $\alpha_{\rm cor}$ for the corona and $\alpha_{\rm ch}$ for the chromosphere. Further, we derive the photospheric distribution of the vertical current density using high-resolution vector magnetograms. The pattern of electric currents shows a mixed distribution of positive and negative currents due to fine spatial structure in the observations, as was reported earlier by Su et al. (2009). We suggest a decomposition method to isolate such strong small-scale electric currents from more uniform currents due to twist of the magnetic field.

The paper is organized as follows. In Section 2 we describe the observational data sets and the method of LFFF modeling. In Section 3 we present the results of the modeling for the two sunspots and deduce the best-fit α values for the two spots. In Section 4 we analyze the photospheric distribution of the vertical current density J_z and then present a new method to decompose J_z in two components in order to filter the large values due to the fibrils. Finally, in Section 5 we discuss the results and give our conclusions.

2. OBSERVATIONS AND MODELING

2.1. Data Analysis

The two sunspots studied here are simple round sunspots; one is identified in the active region (AR) NOAA 11084 (southern hemisphere) and the other one in AR NOAA 11092 (northern hemisphere). Both spots conform to the hemispheric pattern of chirality (Balasubramaniam et al. 2004). These two spots were chosen for our study because (1) they are regular, of round shape with a nearly uniform twist in the azimuthal direction in chromospheric and coronal images; (2) they are isolated and not surrounded by other strong polarities, and therefore of minimal complexity; and (3) they are not involved in flaring activity in the range of times selected for the present analysis.

The contextual pictures (chromospheric, coronal, photospheric continuum, and longitudinal magnetogram) of the two sunspots are displayed in Figure 1. The images shown in this figure were obtained by the instruments Atmospheric Imaging

Assembly (AIA; Lemen et al. 2012) and Helioseismic and Magnetic Imager (HMI; Scherrer et al. 2012) on board the *Solar Dynamics Observatory* (*SDO*) spacecraft (Pesnell et al. 2012).

Further, for high-resolution vector magnetic field data of these sunspots we use observations from Solar Optical Telescope (SOT; Kosugi et al. 2007; Tsuneta et al. 2008) on board the *Hinode* spacecraft. The vector magnetograms are derived by performing Milne–Eddington (M-E) inversion of the spectropolarimetric profiles of the Fe I 630 nm line pair observed by the Spectro-Polarimeter (SP) instrument (Ichimoto et al. 2008) on board *Hinode* SOT. The data reduction and calibration of the Stokes profiles are performed by using *Solarsoft* routines (Lites & Ichimoto 2013), and the retrieval of the magnetic field vector under M-E approximation is carried out by the data analysis pipeline at HAO/CSAC (Community Spectropolarimetric Analysis Center of High Altitude Observatory, Boulder). The data are called *Hinode* level 2 data sets at HAO/CSAC. We estimate the background (quiet-Sun region in the field of view shown in Figure 1) noise in the longitudinal and horizontal component of the magnetic field in these maps to be ≈50 G and ≈120 G, respectively, at 1σ level.

The 180° azimuth ambiguity of the observed magnetic field is easily solved with the acute angle method (Metcalf et al. 2006) as the two sunspots studied here are simple round sunspots. In this method the azimuth solution making acute angle with respect to the potential field azimuth direction is taken as the correct solution. It is known that, except for the highly sheared PILs of complex active regions, the acute-angle method works very well. For a review of azimuth ambiguity resolution algorithms see (Metcalf et al. 2006). The vector magnetograms are then transformed and remapped to the heliographic coordinate system (Venkatakrishnan et al. 1988).

2.2. Linear Force-free Field Modeling

We model the twisted coronal and chromospheric magnetic structures in both ARs assuming the LFFF approximation. To compare the models with observations, we use *SDO*/AIA data taken in the 171 Å and 304 Å wavelength bands (henceforth AIA 171 and AIA 304). The magnetic field models are obtained using a fast Fourier transform (FFT) method described by Alissandrakis (1981), developed by Démoulin et al. (1997), and used in a number of studies (see, e.g., López Fuentes et al. 2006). As boundary conditions for the model we use longitudinal magnetograms from *SDO*/HMI corresponding to the closest time to the AIA observations. The above procedure consists of the extrapolation of the observed photospheric field into the corona following the LFFF equation:

$$\nabla \times \mathbf{B} = \alpha \mathbf{B}. \quad (1)$$

In the case of AR 11084 the size of the extrapolation box is 300 Mm in x, y, and z directions, and it is the same for both wavelengths. The grid has 129 points in x and y (horizontal) directions and 81 points in z (vertical) direction. The grid spacing is not uniform. It is 1 Mm at the center of the x–y plane and the base of the box ($z = 0$) and increases linearly in the vertical and x and y directions. Since the magnetograms have a uniform grid, before the computation the code interpolates the magnetogram pixel values to the above grid points. For AR 11092 it is the same except that the x–y plane size is 350 Mm × 350 Mm.

We obtain magnetic field models with different values of the force-free parameter α and integrate sets of field lines

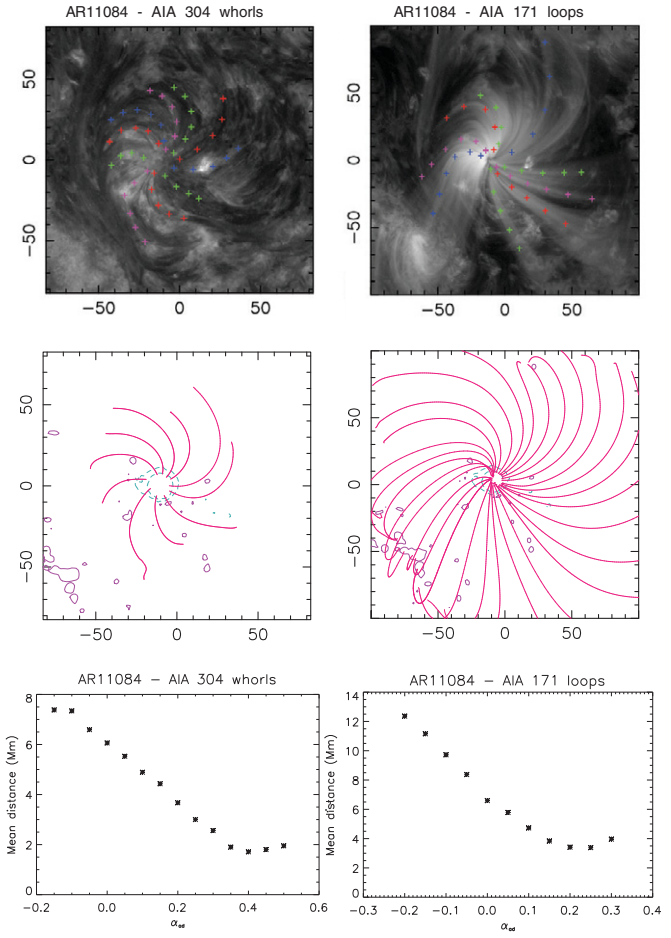

Figure 2. Top row shows, from left to right, the AIA 304 and AIA 171 images of NOAA 11084, with plus signs identifying the selected structures. The middle panels show representative field lines of the best-fit LFFF model corresponding to the structures present in the top row. The units of the x and y axes are Mm. Magenta (green) contours correspond to upward (downward) line-of-sight magnetic field for 100 and 500 G levels. The bottom row shows the curve of the minimization function (mean distance between field lines and observed whorls/loops) for different values of α_{ad} (adimensional α value; see Section 3.1).

(A color version of this figure is available in the online journal.)

that we compare with the structures observed in AIA images. For the comparison we align the model with the data and compute the mean distance from model field lines to selected observed structures, such as EUV loops or chromospheric whirls, depending on the type of data. Each structure is defined by a series of points selected by eye on contrast-enhanced images. These selected structures are represented by colored plus signs in the top panels of Figures 2 and 3. A large number of field lines is computed in the vicinity of each structure. The distance of each field line, projected on the plane of sky, to the structure is computed. The field line minimizing this distance is selected, then new field lines are computed around it, and the procedure is continued until the minimum distance has no significant change. The last identified field line defines the minimum distance to the selected structure. This procedure is applied to an ensemble of structures (loops, fibrils), and a mean distance is defined. Repeating the above analysis for different α values defines the curves shown at the bottom of Figures 2 and 3. A detailed description of this procedure can be found in Green et al. (2002) and López Fuentes et al. (2006).

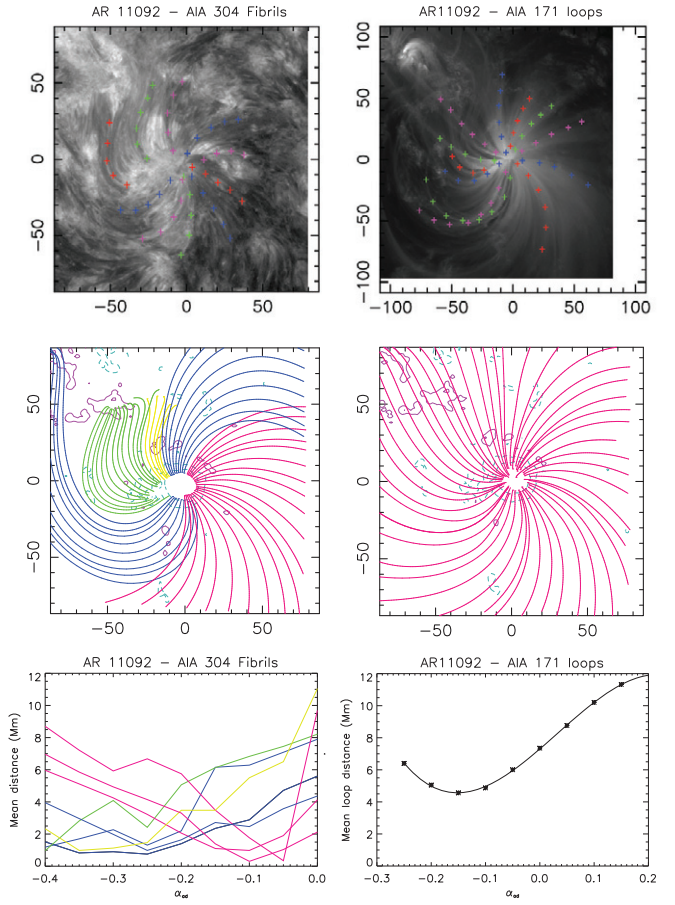

Figure 3. Same as in Figure 2 but for NOAA 11092. The middle left panel shows LFFF model fitting of sets of field lines with different α (shown by different colors) with different α. The corresponding curves of minimization function for these selected structures are plotted in the lower left panel, for different α_{ad} values.

(A color version of this figure is available in the online journal.)

3. RESULTS WITH LFFF MODELS OF AR 11084 AND 11092

3.1. Coronal and Chromospheric LFFF Modeling

In Figure 2 we show the results of LFFF modeling for NOAA 11084. In the top row we show the *SDO*/AIA intensity images in AIA 304 and AIA 171 channels. In the middle row we show a set of model field lines for the best-fit model, and in the bottom row we show the mean distance between model field lines and observed AIA structures in NOAA 11084 for different α values. Here we use an adimensional parameter α_{ad} that is related to α from Equation (1) by $\alpha_{ad} = \alpha 10^8$ m$/2\pi$, where α is in m^{-1}.

We consider the best-fit model as the one that corresponds to the minimum mean distance. As can be seen in the plot, the best fit is obtained for $\alpha_{ad} \approx 0.23$, corresponding to $\alpha_{cor} \approx 1.44 \times 10^{-8}$ m^{-1} for AIA 171, while the best fit of the model field lines to the AIA 304 whorls is obtained for $\alpha_{ad} \approx 0.4$, corresponding to $\alpha_{ch} \approx 2.5 \times 10^{-8}$ m^{-1}.

Similarly, in the case of NOAA 11092 we show results of LFFF modeling in Figure 3. In this case we find the best-fit value of α for AIA 171 to be $\alpha_{ad} \approx -0.15$, corresponding to $\alpha_{cor} \approx -0.94 \times 10^{-8}$m^{-1}. For AIA 304 we observe that the fibrils show different amounts of twist in different sectors, and therefore we try to model different regions around the sunspot separately, as shown in the middle left panel of Figure 3. Different sets of fibrils around the sunspot (shown by different colors) are found to correspond to different values of best-fit α_{ad}. The average value of α_{ad} corresponds to $\alpha_{ch} \approx -1.8 \times 10^{-8}$ m^{-1}, and α_{ch} is in the range $[-2.5, -0.94] \times 10^{-8}$ m^{-1}. The high value of α_{ch} in some parts of the sunspot is in contrast to the coronal AIA 171 loops, which are described by nearby α values.

We conclude that the α values of the magnetic structures depend on height in the solar atmosphere, being larger at chromospheric heights by a factor of two than for coronal loops (Table 1).

Table 1
Force-Free Parameter α

Active Region No.	α_{ph}	α_{ch}	α_{cor}
NOAA 11084	2.4	2.5	1.44
NOAA 11092	−1.0	−1.8 (−2.5,−0.94)	−0.94

Notes. The value of force-free parameter α at different heights, photosphere (α_{ph}), chromosphere (α_{ch}), and corona (α_{cor}) are given. The units are in 10^{-8} m^{-1}. The values in parentheses are the minimum and maximum amplitude of twist deduced by fitting different loops (see lower left panel in Figure 3).

3.2. Best-fit α Parameter for Photosphere: α_{ph}

The best-fit value of α for the photospheric vector field, α_{ph}, can be derived by LFFF computing for different values of α and minimizing the difference between the observed transverse component, $\boldsymbol{B}_{tr,obs}$, and the modeled one $\boldsymbol{B}_{tr,lfff}$ (Pevtsov et al. 1995). More precisely, by minimizing the quantity $(1/N)\sum_{i=1}^{N}(\boldsymbol{B}_{tr,obs} - \boldsymbol{B}_{tr,lfff})^2$, where i is the summation index for all pixels of a given region, we derive the best-fit value α_{ph}. We use the longitudinal component of the *Hinode* vector magnetograms for the LFFF computation. Further, the pixels below the noise level threshold of 120 G for transverse field $\boldsymbol{B}_{tr,obs}$ were excluded in the summation. The best-fit values of α_{ph} that we derive using this method are $\approx 2.4 \times 10^{-8}$ m^{-1} for NOAA 11084 and $\approx -1.0 \times 10^{-8}$ m^{-1} for NOAA 11092. The sign and magnitude of the α_{ph} corresponds well with the best-fit LFFF model in the chromosphere, considering the fact that these are derived independently from two methods and two magnetographs with different types of measurements.

In the case of NOAA 11092, various chromospheric fibrils show different amounts of α (see left middle panel in Figure 3), and so a global best-fit $\alpha_{ph} \approx -1.0 \times 10^{-8}$ m^{-1} might be an underestimate. However, the value of $|\alpha|$ in NOAA 11084 is consistently larger than the twist in NOAA 11092 at all three heights. This inference can also be made visually in AIA 171 images in Figure 1, where, on average, the loops in NOAA 11084 appear more twisted than loops in NOAA 11092 (taking into account that the images have the same field-of-view size).

4. PHOTOSPHERIC ELECTRIC CURRENT MAPS

4.1. Spatial Distribution of Electric Current from High-resolution Vector Magnetograms

The high-resolution photospheric vector magnetograms obtained from *Hinode* SOT/SP observations easily resolve the sunspot fine structures such as the penumbral fibrils (e.g., Figure 4). As a result of the fine structures, the maps of the vertical component of the electric current density J_z thus show strong local currents (Figures 5(d) and 6(d)). Such high-resolution

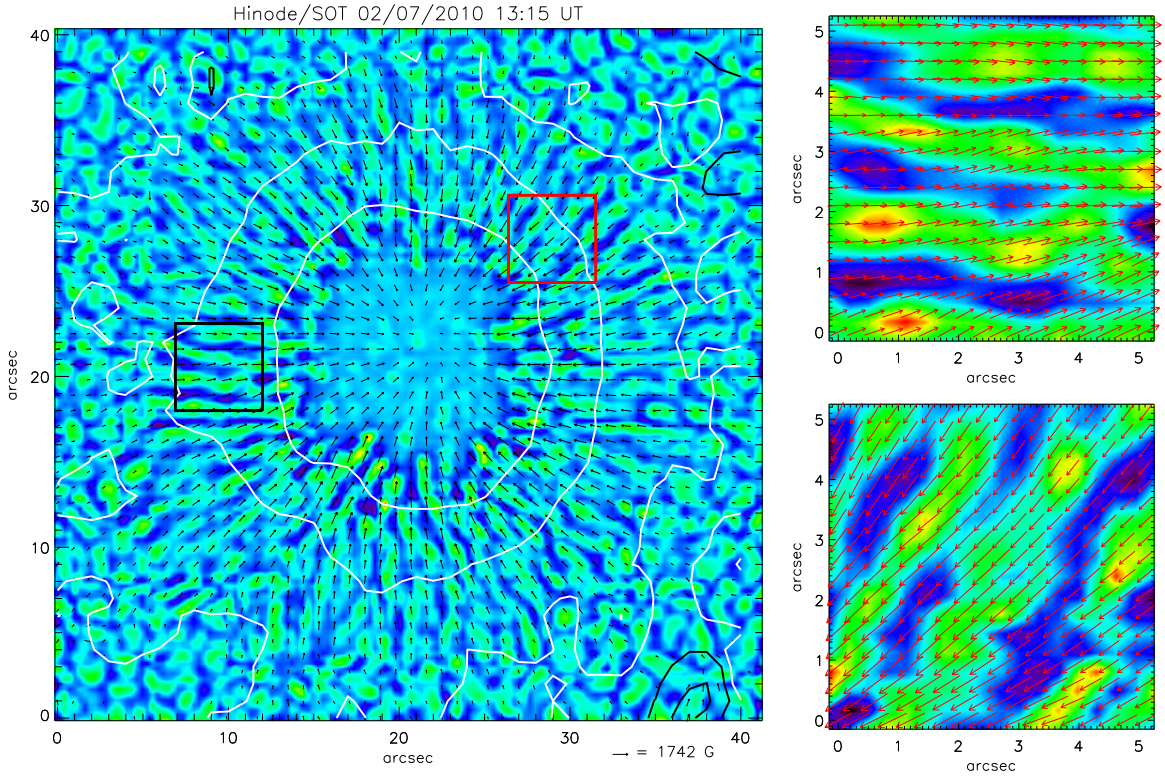

Figure 4. Main panel: high-pass-filtered continuum intensity map from *Hinode* SOT/SP. The white (black) contours show the radial component of the field pointing downward (upward). The contours are drawn at 1500, 1000, and 500 G levels. The arrows show the transverse field vectors where the scaling of arrow length is shown in the lower right bottom of the panel. A zoom-in of the regions inside black and red square boxes is shown in the top and bottom panels, respectively, in the right column.

(A color version of this figure is available in the online journal.)

maps of electric current density and the corresponding map of α parameter show elongated patterns, corresponding to elongated penumbral fine structure, with alternating positive and negative sign, as shown by Su et al. (2009) and Venkatakrishnan & Tiwari (2009).

It is currently well established that the penumbral magnetic field has an azimuthal variation of the zenith angle of a few times 10° on the transverse scale of the fibrils, which can be at arcsecond and even subarcsecond scale (Title et al. 1993; Solanki & Montavon 1993; Martínez Pillet 2000). From Ampere's law, such variations of the magnetic field on short scales imply the presence of strong alternating electric currents as present in the J_z maps. Since these currents are present on small scales, it is quite likely that a large part of these +/− currents close across field lines in the photosphere and chromosphere and do not reach higher up in the corona. The penumbral fibrils have also different densities and hence different opacities (e.g., Puschmann et al. 2010); therefore, $\boldsymbol{B}$ is measured at different heights. It implies a variable measured field strength across the fibrils, so again on short scales. This introduces false strong currents (on top of a possible real one owing to a true variation of the field strength) in the J_z maps.

4.2. Decomposition of the Photospheric Electric Current

The strong electric currents, with alternating positive and negative sign across the penumbral filaments, mask the more distributed and weaker current pattern owing to the global twist of the sunspot magnetic field. In order to remove this "zebra-pattern," one needs to separate the contributions of currents due to spatial structure across the fibrils and the overall twist of the sunspot magnetic field. Such a decomposition can be performed assuming cylindrical symmetry of the sunspots (Venkatakrishnan & Tiwari 2009). In general, however, the fibrils are not exactly radial, and an offset remains between radial direction and fibril elongation direction. In order to avoid this problem, we perform the decomposition of electric current density j_z by taking the derivative along and perpendicular to the fibril direction as described below.

In order to perform such decomposition, we need to estimate the direction of the fibrils. We first tried to define the fibril direction as the normal to the direction of steepest descent in the high-pass-filtered $|\boldsymbol{B}_h|$, as well as the continuum intensity map. However, this led to a lot of noise in the deduced directions, as the computation of the gradient amplifies the fluctuations already seen in the fibril pattern. This procedure is found to be unsatisfactory for current decomposition. We then considered the transverse field direction as an approximation to the fibril orientation. This assumes that the flux tube of each fibril is weakly twisted.

We applied a high-pass filter to enhance the high-frequency component (for, e.g., fibrils) in the image, as shown in the left panel of Figure 4. The fibrils, as seen in the intensity images, are closely aligned with $\boldsymbol{B}_h$. Moreover, the observed horizontal magnetic field, $\boldsymbol{B}_h$, is well resolved and has a coherent direction between adjacent pixels (Figure 4). This is shown more closely in two zoom-in regions, selected as examples and displayed in the adjacent panels on the right. Therefore, in the following the transverse field direction is selected to perform the decomposition of the electric current density j_z.

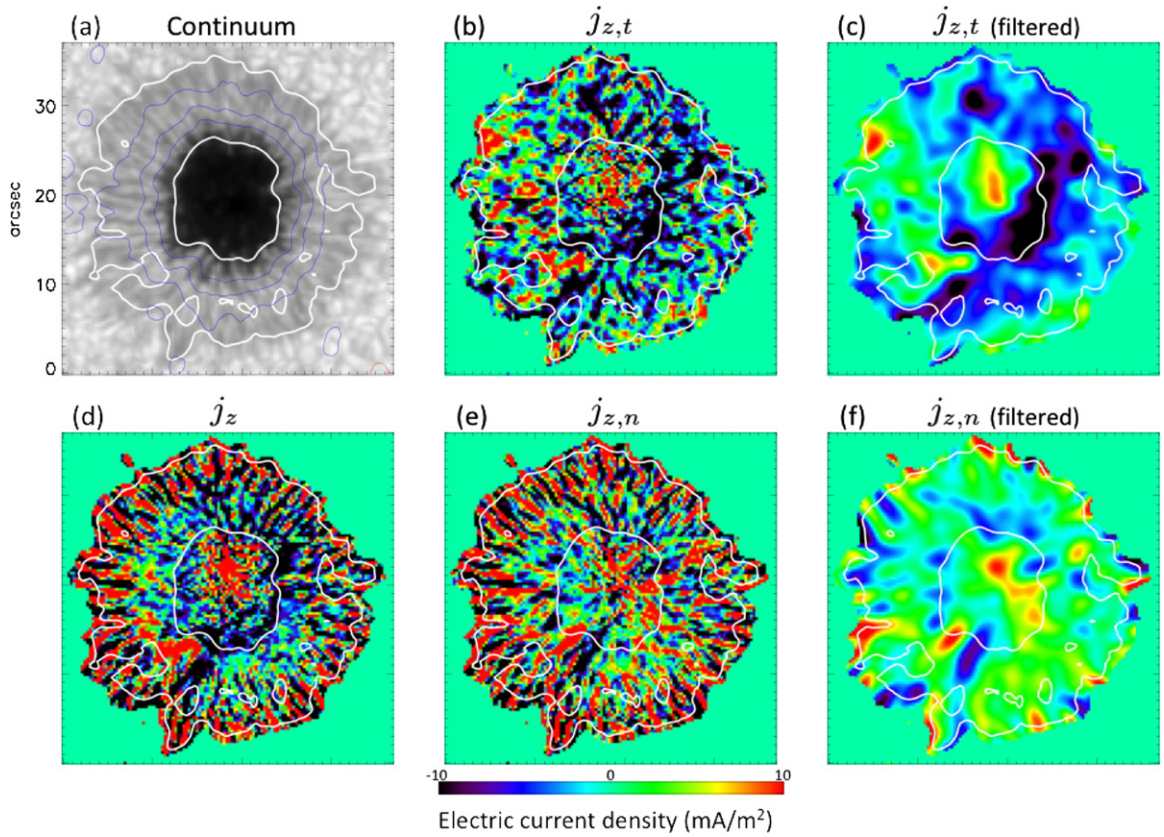

Figure 5. Maps of electric current density derived from *Hinode* SOT/SP vector field observations are shown for NOAA 11084. The top panels show (a) the maps of *Hinode* SOT/SP continuum intensity, (b) electric current density $j_{z,t}$, and (c) low-pass-filtered $j_{z,t}$, respectively. The bottom panels show the maps of (d) j_z, (e) $j_{z,n}$, and (f) low-pass-filtered $j_{z,n}$, respectively. In (a), the blue and red contours mark radial magnetic field pointing downward and upward, respectively. Contours are drawn at 1500, 1000, and 500 G levels. In all panels, the white contours represent the normalized continuum intensity for levels 0.3 and 0.75. The maps for electric current density are scaled between ± 10 mA m^{-2}.

(A color version of this figure is available in the online journal.)

Let us define the unit vector $\hat{t}$ along the horizontal field $\boldsymbol{B}_h$ and its horizontal normal $\hat{n}$ as

$$\hat{t} = \boldsymbol{B}_h / B_h = \cos\psi\ \hat{x} + \sin\psi\ \hat{y} \tag{2}$$

$$\hat{n} = \hat{z} \times \hat{t} = -\sin\psi\ \hat{x} + \cos\psi\ \hat{y}, \tag{3}$$

where $\hat{x}$, $\hat{y}$ are the orthogonal horizontal directions, $\hat{z}$ is the local vertical, $|\hat{t}| = |\hat{n}| = |\hat{x}| = |\hat{y}| = |\hat{z}| = 1$, and ψ is the azimuthal angle between $\hat{x}$ and $\hat{t}$. Then, the vertical current density,

$$\mu_0\ j_z = (\boldsymbol{\nabla} \times \boldsymbol{B}).\hat{z} = (\boldsymbol{\nabla}_h \times (B_h \hat{t})).\hat{z}\,, \tag{4}$$

is decomposed as the sum of two contributions computed with spatial derivatives along and orthogonal to $\boldsymbol{B}_h$ as

$$\mu_0\ j_z = \mu_0\ j_{z,t} + \mu_0\ j_{z,n} \tag{5}$$

with

$$\mu_0\ j_{z,t} = \left(\hat{t}\frac{\partial}{\partial t} \times \boldsymbol{B}_h\right).\hat{z} = \boldsymbol{B}_h.\boldsymbol{\nabla}\psi \tag{6}$$

$$\mu_0\ j_{z,n} = \left(\hat{n}\frac{\partial}{\partial n} \times \boldsymbol{B}_h\right).\hat{z} = -\hat{n}.\boldsymbol{\nabla}B_h. \tag{7}$$

The derivation of the right-hand sides of Equations (6) and (7) is given in the Appendix. Equation (6) implies that $j_{z,t}$ is only due to the variation of the azimuth angle, ψ, along the horizontal magnetic field, $\boldsymbol{B}_h$, while Equation (7) implies that $j_{z,n}$ is only due to the change of the horizontal field strength orthogonal to $\boldsymbol{B}_h$.

The above decomposition, Equation (4), splits the current density into two parts without loss of signal, in contrast to the application of a spatial filter where some signal is lost. However, it is worth remembering that both $j_{z,t}$ and $j_{z,n}$ contain large-scale currents that are expected to flow into the corona. Indeed, $j_{z,n}$ is designed to keep most of the current coming from the fibril structure, but it still contains a part of nonfibril currents. In order to better visualize the distribution of these last currents, one can apply a low-pass filter to $j_{z,n}$. A similar filtering can be applied to $j_{z,t}$ to further remove the remaining fibril contribution. The interest of the decomposition is to keep the highest possible spatial resolution on the part of j_z, which is less affected by the fibril pattern, i.e., $j_{z,t}$, rather than applying a strong low-pass filter to j_z. Such filtering is only an optional last step of the proposed method. It allows us to better visualize the weak large-scale current densities.

4.3. Pattern of j_z versus $j_{z,t}$ in Twisted Sunspots

In Figures 5 and 6 maps of continuum intensity and electric current density are shown. The maps of $j_{z,t}$ and low-pass-filtered $j_{z,t}$ (henceforth $j^f_{z,t}$) are shown in the top panels, while the maps of j_z, $j_{z,n}$, and low-pass-filtered $j_{z,n}$ (henceforth $j^f_{z,n}$) are shown in the bottom panels. $j_{z,t}$ and $j_{z,n}$ are

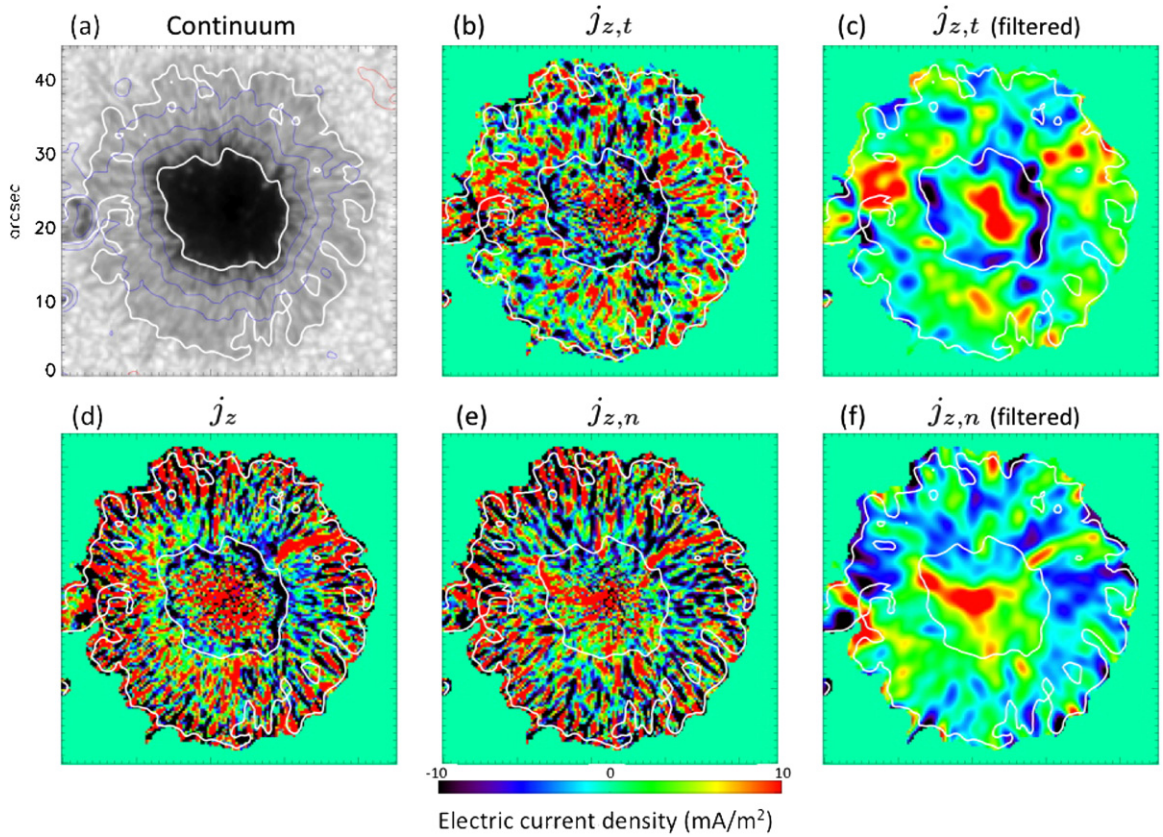

Figure 6. Same as Figure 5, but for NOAA 11092.
(A color version of this figure is available in the online journal.)

Table 2
The Current Imbalance (CI)

Active Region No.	J_z	$J_{z,t}$	$J_{z,n}$	$J^f_{z,t}$	$J^f_{z,n}$	$\Sigma\|J_z\|$	$\Sigma\|J_{z,t}\|$	$\Sigma\|J_{z,n}\|$	$\Sigma\|J^f_{z,n}\|$
NOAA 11084	−11%	−34%	9%	−69%	38%	5.3	3.1	4.9	1.2
NOAA 11092	9%	14%	−1%	33%	−1.3%	7.4	5.0	6.9	2.2

Notes. The current imbalance, CI(%)=$\Sigma_i j/\Sigma_i |j|$, is given in Columns 2–6. The summation is done over all the pixels above the noise threshold, as shown in Figures 5 and 6. The total unsigned current (in units of 10^{12} A) for the maps is given in Columns 7–10.

computed with the expressions written in Cartesian coordinates (Equations (A11) and (A12)). The electric current density in all the maps is scaled between ± 10 mA m^{-2} so that they are directly comparable.

The j_z map of the NOAA 11084 spot has elongated alternate ± currents, and they are dominant over the penumbral region owing to the presence of penumbral fibrils (Figure 5(d)). However, after the decomposition of j_z into $j_{z,t}$ and $j_{z,n}$, the map of $j_{z,t}$ is almost free from this elongated ± current pattern (Figure 5(b)). This is even clearer in the $j^f_{z,t}$ (Figure 5(c)), which has mostly negative values. On the other hand, the map of $j_{z,n}$ (Figure 5(e)) mostly contains the elongated ± current pattern due to the penumbral fibrils. Only weak currents remain on the low-pass-filtered $j^f_{z,n}$ map (Figure 5(f)) as quantified in Table 2 by the comparison of $\Sigma|J^f_{z,n}|$ with $\Sigma|J_z|$. Thus, in this case the decomposition of j_z succeeds in keeping most of the fibril pattern in $j_{z,n}$ maps even if the twist of $\boldsymbol{B}_h$ is weak, as the magnetic field is mostly radial within the sunspot penumbra (Figure 4).

Similarly, in Figure 6 maps of electric current density are shown for the NOAA 11092 spot. Here, again dominant alternating ± currents are present in the penumbral region in the j_z map (Figure 6(d)). After the decomposition, the ± current pattern is mostly present in $j_{z,n}$, but a part is still present in $j_{z,t}$ (Figure 6(b)). These remaining ± current patterns are mostly removed in the low-pass-filtered $j^f_{z,t}$ (Figure 6(c)). The corresponding filtered $j^f_{z,n}$ (Figure 6(f)) contains more currents than the previous case (Figure 5(f) and Table 2).

While the decomposition of j_z provides comparable results for both spots, the decomposition has more difficulties in separating the fibril pattern from other currents for the second case. Indeed, the currents are stronger for NOAA 11084 than for NOAA 11092 (compare panels c and f of Figures 5 and 6). This is in agreement with the results of Section 3: both LFFF modeling and visual inspection of coronal and chromospheric structures show that twist is lower in NOAA 11092. It implies that the fibril pattern is even more dominant on the distributed current in case of NOAA 11092 and the j_z decomposition has more difficulties in separating it from other currents (Figure 6).

Further, in NOAA 11084 the dominant current is negative, while in NOAA 11092 the dominant current is positive. This is confirmed by a spatial integration of j_z. This is also true for

$j_{z,t}$; however, for $j_{z,n}$ the dominant current sense is opposite in the two spots, i.e., positive in NOAA 11084 and negative in NOAA 11092. More precisely, we define the current imbalance (CI) as $100 \times \text{total}(j)/\text{total}(|j|)$. The results are summarized in Table 2. We conclude that the imbalance increases for filtered cases. Moreover, the imbalance is stronger for $j_{z,t}$ and $j^f_{z,t}$, and they are coherent with the dominance of j_z.

Since both the sunspots are of negative magnetic polarity, i.e., $B_z < 0$, this means that the electric currents are flowing dominantly parallel and anti-parallel to the magnetic field in NOAA 11084 and NOAA 11092, respectively. This is in agreement with the chirality of the coronal and chromospheric structures seen in the AIA images for these two sunspots (Figure 1).

4.4. Detection of Return Currents

The distribution of $j_{z,t}$ in Figures 5(b) and 5(c) has a global negative distribution with a concentrated positive current near the sunspot center. A similar pattern is present in the low-pass-filtered $j^f_{z,n}$ (Figure 5(f)). Indeed, the real j_z currents have a contribution in both $j_{z,t}$ and $j_{z,n}$, so that related patterns are expected, but we cannot exclude also the effect of imperfect decomposition of j_z. The distribution of $j_{z,t}$ in Figures 6(b) and (c) has a comparable distribution, but with a more extended and stronger positive core, while the surrounding annular negative current is less extended and weaker. A comparable pattern, while not complete and more fragmented, also seems to be present in the low-pass-filtered $j^f_{z,n}$ (Figure 6(f)). Such a ring-like pattern of oppositely directed electric currents at the umbra-penumbra boundary was also reported in Su et al. (2009) in a different sunspot; however, this was not investigated in detail. Finally, both the central positive current and its surrounding negative annular current pattern could be distinguished from the +/− fibril pattern in both j_z maps of the spots (Figures 5(d) and 6(d)), so that both spots seem to have a similar current pattern in j_z maps in contradiction with the opposite chirality observed in the chromospheric and coronal AIA images (Figure 1)!

Opposite currents are indeed expected to be present in flux ropes within the convective zone, as their magnetic field is confined to a small volume in a mostly field-free plasma (Parker 1996), as follows. If the flux rope has a finite total net current, then Faraday's law implies that its azimuthal field decreases inversely to the distance to the flux-rope axis. This is too slow a decrease, and indeed a twisted flux rope confined to finite volume needs a return electric current around its core that would cancel the core electric current. This return current can have a volume distribution, or it can be a current layer at the flux-rope boundary. However, it is not currently settled how far this return current can go in the solar atmosphere, as it may flow across field lines at and around the photospheric region as the magnetic field expands and fills all the available space (e.g., Longcope & Welsch 2000; Török et al. 2014). An annulus of return currents is also naturally formed when a twisting motion of finite extension is applied to an untwisted magnetic field. However, neutralization is only partial in a bipolar field if a finite magnetic shear is present along the photospheric inversion line between the two magnetic polarities (Aulanier et al. 2005).

The j_z maps of the spots (Figures 5(d) and 6(d)) seem to both indicate the presence of a central positive current surrounded by an annulus of negative current as expected theoretically with a localized twisted flux rope. Since $B_z < 0$ for both spots, it would imply a negative helicity, in contradiction with a positive chromospheric and coronal helicity for NOAA 11084. The decomposition of j_z allows us to solve this paradox as $j_{z,t}$ maps show only a weak positive central current (Figures 5(b) and 5(c)) while only mixed currents remain in $j_{z,n}$ maps (Figures 5(e) and (f)). The direct current for this spot is in fact negative, and no significant positive return current is detected around it (see Section 4.3). The second spot shows a more expected current pattern (Figure 6). The negative return current is well imaged, as it is strong and around the umbra/penumbra boundary.

5. DISCUSSION AND CONCLUSIONS

In the present study we analyzed two simple round sunspots for which the coronal and chromospheric images show nearly uniformly twisted structures tracing a whirly pattern. The two sunspots were relatively quiet regions, with no major flaring activity associated with them. Further, the two spots were located in opposite hemispheres, and the one in the northern hemisphere, NOAA 11092, showed counterclockwise (CCW) whirls, while the one in the southern hemisphere, NOAA 11084, showed clockwise (CW) whirls. Therefore, these spots belong to the dominant helicity sign present in each hemisphere (Hale 1927; Pevtsov et al. 1994; Gosain et al. 2013).

The twist of these structures, i.e., the coronal loops and chromospheric fibrils, as seen in the *SDO*/AIA images was modeled using the LFFF extrapolation method. The best-fit values of the linear force-free parameter shows that structures in the chromosphere are more twisted than in the corona by a factor of two (Figures 2 and 3). One possible explanation is that these observed chromospheric structures, i.e., super-penumbral fibrils, retain more of the original twist built in the convective zone, as they are less implied in flares and coronal mass ejections. Another, simpler explanation is linked to the extension of the field lines, as follows. In ideal MHD, and assuming no new helicity injection, if the length of a twisted loop doubles, its total twist is constant, implying that α decreases by a factor of two, for example. Coronal loops are much more extended than chromospheric structures, so they are expected to have a weaker α value, as is indeed observed here.

Next, we derive the photospheric linear force-free parameter, $\alpha_{\rm ph}$, by least-squares fitting the observed horizontal magnetic field with an LFFF. We obtain $\alpha_{\rm ph}$ values that are consistent with the values obtained in the chromosphere by the LFFF modeling of the chromospheric structures.

Further, we used high-resolution vector magnetograms from *Hinode* to study the distribution of vertical current density, j_z. The small-scale features in the sunspot, such as the penumbral fibrils, are resolved by *Hinode*. They are associated with strong local currents because the fibril pattern introduces small scales in the direction transverse to the fibrils and j_z is computed from spatial derivatives of the horizontal magnetic field $\boldsymbol{B}_h$. A part of these currents are due to the uncombed magnetic fields of the penumbra, which are mostly present at the photospheric and chromospheric levels. Another part is expected to be due to variation of optical opacity across the fibrils, which implies that the magnetic field is measured at a variable height. This introduces an artificial modulation of $\boldsymbol{B}_h$. In both cases, the small-scale variation of $\boldsymbol{B}_h$ across the fibrils introduces a strong zebra pattern of alternating positive and negative currents that are masking more distributed and weaker currents. Such larger-scale currents are expected to enter in the corona, and so they are at the origin of the observed twisted coronal structures.

A decomposition of j_z was performed to isolate the currents dominated by the small-scale fibrils. This is realized by

separating the derivatives in the $\nabla \times \boldsymbol{B}_h$ in derivatives tangent and normal to $\boldsymbol{B}_h$. It decomposes j_z maps in $j_{z,t}$ and $j_{z,n}$ maps, respectively (Figures 2 and 3). This decomposition is general and so could be applied to any vector magnetogram (see the Appendix). We show in two sunspot examples that indeed $j_{z,n}$ maps kept most of the zebra pattern of alternating positive and negative currents, while $j_{z,t}$ has more distributed currents owing to global twist of the sunspot. This decomposition preserves the currents as $j_z = j_{z,t} + j_{z,n}$.

The two analyzed sunspots have, at first, similar j_z maps with a central positive current, surrounded by an annulus of dominantly negative current, then another annulus of strong mixed-polarity currents (in the penumbra; Figures 2 and 3). Both sunspots have a negative magnetic polarity ($B_z < 0$), and then the sunspots have apparently the same magnetic chirality, in contradiction with the chromospheric and coronal observations. However, the j_z decomposition shows that the sunspot of NOAA 11084 has mostly negative distributed current in $j_{z,t}$ maps. This shows that this sunspot has positive helicity, in contrast to the false impression given by the j_z map but in agreement with chromospheric and coronal observations. For the other analyzed sunspot, in NOAA 11092, all analyses agree on a negative helicity. Here the j_z decomposition allows us to better identify the central positive current from its surrounding annulus with negative current located around the umbra/penumbra boundary. These direct and return currents are best seen in the $j_{z,t}$ map and are only partially present in the highly filtered $j_{z,n}$ maps.

In conclusion, the twist of photospheric magnetic field and the overlying coronal and chromospheric structures are basically consistent with each other, apart from a factor of two on the magnitude of α. Our new decomposition method provides a way to isolate the strong small-scale currents from the weaker large-scale currents, which originate from the overall twist of the sunspot magnetic field. The small-scale currents of mixed polarity do not contribute to building a large-scale twisted field; moreover, some of them are expected to be fake, owing to opacity variations. However, all these small-scale currents provide a challenge to magnetic extrapolations as they occur at or close to the pixel size while the numerical methods are solving equations involving spatial derivatives of the magnetic field. Since the observed zebra patterns are not expected to contribute significantly to the coronal field and they are an obstacle for numerical methods, we propose that the above j_z decomposition be part of the preprocessing of vector magnetograms.

The authors thank the *Hinode* SOT, HAO/CSAC, and *SDO* teams for providing the data sets online. M.L.F. acknowledges financial support from Argentinean grants PICT 2007-1790 (ANPCyT), UBACyT 20020100100733, and PIP 2009-100766 (CONICET). M.L.F. is a member of the Carrera del Investigador Cientifico (CONICET).

APPENDIX

DECOMPOSITION OF THE CURRENT DENSITY

The current density j_z is computed from derivatives of the horizontal magnetic field $\boldsymbol{B}_h$. A fibril pattern is typically observed in intensity at the photospheric level where magnetic field is measured. It is dominant in the penumbra of the spots (Figure 4). This fibril pattern introduces small scales transverse to the fibrils that are mostly along $\boldsymbol{B}_h$. It implies a pattern of alternating positive and negative current densities in j_z maps (Figures 5(d) and 6(d)). These large current densities mask the more distributed currents that are expected to enter the corona. Below we derived a method to separate most of these strong currents due to the fibril pattern from the j_z maps. A Cartesian orthonormal frame $(\hat{x}, \hat{y}, \hat{z})$ is used where the magnetogram is in the x, y-plane.

The vertical current density j_z is directly computed from the horizontal derivative, ∇_h, of the horizontal magnetic field $\boldsymbol{B}_h = B_h \hat{t}$. We decompose it in a contribution due to derivative parallel, $j_{z,t}$, and perpendicular, $j_{z,n}$, to $\boldsymbol{B}_h$ as

$$\mu_0\, j_z = (\nabla \times \boldsymbol{B}).\hat{z} = (\nabla_h \times \boldsymbol{B}_h).\hat{z} = \mu_0\,(j_{z,t} + j_{z,n}) \quad \text{(A1)}$$

with

$$\mu_0\, j_{z,t} = \left(\hat{t}\frac{\partial}{\partial t} \times \boldsymbol{B}_h\right).\hat{z} = \left(\hat{t} \times \frac{\partial B_h \hat{t}}{\partial t}\right).\hat{z} \quad \text{(A2)}$$

$$\mu_0\, j_{z,n} = \left(\hat{n}\frac{\partial}{\partial n} \times \boldsymbol{B}_h\right).\hat{z} = \left(\hat{n} \times \frac{\partial B_h \hat{t}}{\partial n}\right).\hat{z}, \quad \text{(A3)}$$

where the horizontal normal, $\hat{n}$, to $\boldsymbol{B}_h$ is defined as

$$\hat{n} = \hat{z} \times \hat{t} \quad \text{(A4)}$$

with $|\hat{t}| = |\hat{n}| = |\hat{z}| = 1$. Here t and n are coordinates parallel and orthogonal to $\boldsymbol{B}_h$, and the partial derivatives along and across $\boldsymbol{B}_h$ are expressed by $\partial/\partial t$ and $\partial/\partial n$, respectively.

We define the azimuthal angle ψ between $\hat{t}$ and the horizontal $\hat{x}$-direction, and then $\hat{t}$ and $\hat{n}$ are written as

$$\hat{t} = \boldsymbol{B}_h/B_h = \cos\psi\ \hat{x} + \sin\psi\ \hat{y} \quad \text{(A5)}$$

$$\hat{n} = \hat{z} \times \hat{t} = -\sin\psi\ \hat{x} + \cos\psi\ \hat{y}. \quad \text{(A6)}$$

The derivatives of $\hat{t}$ parallel and orthogonal to $\boldsymbol{B}_h$ are

$$\frac{\partial \hat{t}}{\partial t} = \frac{\partial \psi}{\partial t}\frac{\partial \hat{t}}{\partial \psi} = \frac{\partial \psi}{\partial t}\hat{n} \quad \text{(A7)}$$

$$\frac{\partial \hat{t}}{\partial n} = \frac{\partial \psi}{\partial n}\frac{\partial \hat{t}}{\partial \psi} = \frac{\partial \psi}{\partial n}\hat{n}. \quad \text{(A8)}$$

With the above equations $\mu_0\, j_{z,t}$ and $\mu_0\, j_{z,n}$ are rewritten as

$$\begin{aligned}\mu_0\, j_{z,t} &= \left(\hat{t} \times \frac{\partial B_h \hat{t}}{\partial t}\right).\hat{z} = \left(\hat{t} \times \left(\frac{\partial B_h}{\partial t}\hat{t} + B_h\frac{\partial \hat{t}}{\partial t}\right)\right).\hat{z} \\ &= B_h(\hat{t} \times \hat{n}).\hat{z}\,\frac{\partial \psi}{\partial t} = B_h\frac{\partial \psi}{\partial t} = \boldsymbol{B}_h.\nabla\psi \end{aligned} \quad \text{(A9)}$$

$$\begin{aligned}\mu_0\, j_{z,n} &= \left(\hat{n} \times \frac{\partial B_h \hat{t}}{\partial n}\right).\hat{z} = \left(\hat{n} \times \left(\frac{\partial B_h}{\partial n}\hat{t} + B_h\frac{\partial \hat{t}}{\partial n}\right)\right).\hat{z} \\ &= (\hat{n} \times \hat{t}).\hat{z}\,\frac{\partial B_h}{\partial n} = -\frac{\partial B_h}{\partial n} = -\hat{n}.\nabla B_h. \end{aligned} \quad \text{(A10)}$$

This demonstrates Equations (6) and (7). It is worth noting that there is no contribution of $\partial\psi/\partial n$ and $\partial B_h/\partial t$ in Equations (A9) and (A10), and j_z has only the contribution of a variable azimuthal angle, ψ, along $\boldsymbol{B}_h$ and a variable field strength, B_h across $\boldsymbol{B}_h$. The above results can be verified by inserting B_x and B_y, deduced from Equation (A5), in $(\nabla \times \boldsymbol{B}).\hat{z} = ((\partial B_y/\partial x) - (\partial B_x/\partial y))$. It also implies

$\mu_0\ j_z = \boldsymbol{B}_h.\boldsymbol{\nabla}\psi - \hat{n}.\boldsymbol{\nabla}B_h$, but without identifying the origin of both terms (parallel and orthogonal derivatives).

Next, for application to data, we write explicitly the components in Cartesian coordinates (x, y), with $\hat{t} = (t_x, t_y)$ and $\hat{n} = (-t_y, t_x)$. The following expressions are easier to code and do not require a special treatment for an artificial jump of ψ (e.g., between 0 and 2π). The partial derivatives are expanded as

$$\frac{\partial}{\partial t} = \hat{t}.\boldsymbol{\nabla} = t_x\frac{\partial}{\partial x} + t_y\frac{\partial}{\partial y}$$
$$\frac{\partial}{\partial n} = \hat{n}.\boldsymbol{\nabla} = -t_y\frac{\partial}{\partial x} + t_x\frac{\partial}{\partial y}$$

and the expressions of the current densities $j_{z,t}$ and $j_{z,n}$ are explicitly written as

$$\mu_0\ j_{z,t} = \left(\hat{t}\frac{\partial}{\partial t} \times \boldsymbol{B}_h\right).\hat{z} = t_x\frac{\partial B_y}{\partial t} - t_y\frac{\partial B_x}{\partial t}$$
$$= t_x^2\frac{\partial B_y}{\partial x} + t_x t_y\left(\frac{\partial B_y}{\partial y} - \frac{\partial B_x}{\partial x}\right) - t_y^2\frac{\partial B_x}{\partial y} \qquad \text{(A11)}$$

$$\mu_0\ j_{z,n} = \left(\hat{n}\frac{\partial}{\partial n} \times \boldsymbol{B}_h\right).\hat{z} = -t_y\frac{\partial B_y}{\partial n} - t_x\frac{\partial B_x}{\partial n}$$
$$= t_y^2\frac{\partial B_y}{\partial x} - t_x t_y\left(\frac{\partial B_y}{\partial y} - \frac{\partial B_x}{\partial x}\right) - t_x^2\frac{\partial B_x}{\partial y}. \qquad \text{(A12)}$$

One verifies that $\mu_0\ (j_{z,t} + j_{z,n}) = ((\partial B_y/\partial x) - (\partial B_x/\partial y)) = \mu_0\ j_z$ so that no current is lost in the decomposition.

REFERENCES

Abramenko, V. I., Wang, T., & Yurchishin, V. B. 1996, SoPh, 168, 75
Alissandrakis, C. E. 1981, A&A, 100, 197
Aulanier, G., Démoulin, P., & Grappin, R. 2005, A&A, 430, 1067
Balasubramaniam, K. S., Pevtsov, A., & Rogers, J. 2004, ApJ, 608, 1148
Bao, S., & Zhang, H. 1998, ApJL, 496, L43
Burnette, A. B., Canfield, R. C., & Pevtsov, A. A. 2004, ApJ, 606, 565
Chae, J., Moon, Y.-J., Rust, D. M., Wang, H., & Goode, P. R. 2003, JKAS, 36, 33
Démoulin, P., Hénoux, J. C., Mandrini, C. H., & Priest, E. R. 1997, SoPh, 174, 73
Gary, G. A. 2001, SoPh, 203, 71
Gosain, S., Pevtsov, A. A., Rudenko, G. V., & Anfinogentov, S. A. 2013, ApJ, 772, 52
Green, L. M., López Fuentes, M., Mandrini, C., et al. 2002, SoPh, 208, 43
Green, L. M., Kliem, B., & Wallace, A. J. 2011, A&A, 526, A2
Hale, G. E. 1927, Natur, 119, 708
Harvey, J. W. 2012, SoPh, 280, 69
Ichimoto, K., Lites, B., Elmore, D., et al. 2008, SoPh, 249, 233
Kosugi, T., Matsuzaki, K., Sakao, T., et al. 2007, SoPh, 243, 3
Lemen, J. R., Title, A. M., Akin, D. J., et al. 2012, SoPh, 275, 17
Lin, H., Penn, M. J., & Tomczyk, S. 2000, ApJL, 541, L83
Lites, B. W., & Ichimoto, K. 2013, SoPh, 283, 601
Longcope, D. W., & Welsch, B. T. 2000, ApJ, 545, 1089
López Fuentes, M. C., Klimchuk, J. A., & Démoulin, P. 2006, ApJ, 639, 459
Mandrini, C. H., Démoulin, P., van Driel-Gesztelyi, L., et al. 2004, Ap&SS, 290, 319
Mandrini, C. H., Pohjolainen, S., Dasso, S., et al. 2005, A&A, 434, 725
Martínez Pillet, V. 2000, A&A, 361, 734
Metcalf, T. R., Leka, K. D., Barnes, G., et al. 2006, SoPh, 237, 267
Nakagawa, Y., Raadu, M. A., Billings, D. E., & McNamara, D. 1971, SoPh, 19, 72
Nakwacki, M., Dasso, S., Démoulin, P., Mandrini, C. H., & Gulisano, A. M. 2011, A&A, 535, A52
Parker, E. N. 1984, ApJ, 283, 343
Parker, E. N. 1996, ApJ, 471, 485
Pesnell, W. D., Thompson, B. J., & Chamberlin, P. C. 2012, SoPh, 275, 3
Pevtsov, A. A., Canfield, R. C., & McClymont, A. N. 1997, ApJ, 481, 973
Pevtsov, A. A., Canfield, R. C., & Metcalf, T. R. 1994, ApJL, 425, L117
Pevtsov, A. A., Canfield, R. C., & Metcalf, T. R. 1995, ApJL, 440, L109
Puschmann, K. G., Ruiz Cobo, B., & Martínez Pillet, V. 2010, ApJ, 720, 1417
Ravindra, B., Venkatakrishnan, P., Tiwari, S. K., & Bhattacharyya, R. 2011, ApJ, 740, 19
Rust, D. M., & Kumar, A. 1996, ApJL, 464, L199
Scherrer, P. H., Schou, J., Bush, R. I., et al. 2012, SoPh, 275, 207
Schmidt, H. U. 1964, NASSP, 50, 107
Seehafer, N. 1990, SoPh, 125, 219
Semel, M. 1967, AnAp, 30, 513
Solanki, S. K., & Montavon, C. A. P. 1993, A&A, 275, 283
Spruit, H. C. 1979, SoPh, 61, 363
Su, J. T., Sakurai, T., Suematsu, Y., Hagino, M., & Liu, Y. 2009, ApJL, 697, L103
Title, A. M., Frank, Z. A., Shine, R. A., et al. 1993, ApJ, 403, 780
Török, T., Leake, J. E., Titov, V. S., et al. 2014, ApJL, 782, L10
Tsuneta, S., Ichimoto, K., Katsukawa, Y., et al. 2008, SoPh, 249, 167
Venkatakrishnan, P., Hagyard, M. J., & Hathaway, D. H. 1988, SoPh, 115, 125
Venkatakrishnan, P., & Tiwari, S. K. 2009, ApJL, 706, L114
Wheatland, M. S. 2000, ApJ, 532, 616